doi: 10.1021/acsaem.9b00860

Hydrogen Bubble Templating of Fractal Ni catalyst for Water Oxidation in Alkaline Media

M. Hao[1], V. Charbonneau[1], N. N. Fomena[1], J. Gaudet[1], D. R. Bruce[2], S. Garbarino[1], D. A. Harrington[3] and D. Guay[1]*

[1] Institut national de la recherche scientifique
Énergie, matériaux et télécommunications (INRS - EMT)
1650 Lionel Boulet Blvd.
Varennes, QC Canada J3X 1S2

[2] ZincNyx Energy Solutions Inc.
8765 Ash Street – Unit 1
Vancouver, BC Canada V6P 6T3

[3] Department of Chemistry,
University of Victoria, PO Box 1700,
Victoria, BC, Canada V8W 2Y2

* Corresponding author Email: guay@emt.inrs.ca

Abstract

Dynamic hydrogen bubble templating of Ni (Ni_{DHBT}) electrodes was used to prepare highly porous films with enhanced properties towards the oxygen evolution reaction (OER). Upon varying the electrodeposition conditions, Ni films with a macroporous primary structure and highly porous cauliflower-like secondary structure were formed. These films are able to develop an extended electrochemically active surface area, up to 270-fold increase compared to Ni plate. They exhibit stable overpotential (η_{250} = 540 mV) at j = 250 mA $cm^{-2}_{geometric}$ in 1M KOH electrolyte, which is 300 mV less positive than at Ni plate. Fe incorporation onto these Ni_{DHBT} structures can further lower OER overpotentials to η_{250} = 310 mV. Ni_{DHBT} films are remarkably stable over prolonged polarization and are characterized by a low Tafel slope (29 mV/ decade) that extends up to j =100 mA $cm^{-2}_{geometric}$, attributed to both superaerophobic characteristics with a contact angle of c*a* 160° between the surface and an air bubble and superhydrophilic characteristics with less than 25° between the surface and a water droplet.

Keywords: Nickel, Iron, macroporous, alkaline, oxygen evolution, superaerophobicity, superhydrophilicity

1. Introduction

Electrochemical water splitting is a promising approach to provide clean and storable chemical fuels (H_2 and O_2). When connected to renewable energy sources whose production is intermittent, water electrolyzers can play a fundamental role in the development of a sustainable energy network. Several approaches to water splitting catalytic processes – such as microbial, photo and photo-electro - still present sluggish oxygen evolution reaction (OER) kinetics that limits the overall efficiency of the process. Recently, there has been a renewed interest in the study of materials exhibiting good activity and stability for the OER. Among OER materials, oxide compounds are the most active,[1] notably binary noble metal oxides[2] (Ru, Ir) and those having complex structures (perovskite,[3] spinel,[4] layered[5]). Nevertheless, in strongly alkaline media (pH ≥13), Ni metallic alloys continue to attract a lot of attention with recent promising achievements in terms of sustained activity.[6]

In combination with improving the intrinsic catalytic properties of OER catalysts, micro-structuring and nano-engineering of the electrode surface are also mandatory. Indeed, micro-structuring helps to increase the number and surface density of reactive sites having good electronic connectivity to the underlying substrate and easy access to the electrolyte, while nano-engineering of the electrode surface facilitates the escape of gas bubbles. The latter aspect is particularly important for applications and device operation in practical electrolysis conditions ($j \geq 100$ mA cm^{-2}). Indeed, the release of O_2 bubbles at large current density is known to alter the reaction efficiency due to overpotentials associated with greater bubble resistance.[7] The mechanisms responsible for this increased inefficiency include bubble formation leading to a net decrease of the available underlying catalytic Ni sites; O_2 bubbles coalescing near the Ni surface which may also cause large ohmic losses due to the formation of non-conductive gas layers; and pH modification (increase) which may lead to possible instability of the catalyst's corrosion processes. In this context, it is of utmost importance to

facilitate the release of gas bubbles from the surface of electrodes participating in gas evolving reactions like oxygen evolution.

The size, size distribution, adsorption, and residency time of gas bubbles on the electrodes can be varied through ultra-gravity [8,9,10] and ultrasonic treatment, [11] leading to decreased overpotentials and increased current density. However, these methods are difficult to implement in industrial production and not cost-effective for commercial systems. More recently, it was reported that passive control of the bubble behavior can be accomplished through nano-engineering of the electrode surface to impart intrinsically active materials with carefully tailored porosity that facilitate the detachment of oxygen bubbles from the surface and, in turn, improved the extrinsic (overall) performances of electrodes. These electrodes are termed "superaerophobic" as gas bubbles trapped at their surfaces typically exhibit very large contact angles. [12] In the literature, several oxides and hydroxides containing various amounts of Ni, Co, Fe and Zn superaerophobic electrodes with nano-engineered surface have shown improved OER characteristic. [13-17] This improvement of the extrinsic properties of electrodes for gas evolving reactions through nano-engineering of the electrode surface is not restricted to the OER and was also observed for other reactions, such as hydrogen evolution.[18-20] Indeed, our ability to prepare materials and electrodes with optimized porosity has reignited interest in research areas involving Li batteries,[21] capacitors,[22] sensors,[23] and catalysis.[24] However, in most of these studies, the materials investigated and the methods used to impart the necessary nano-engineered characteristics to the electrode surface are not relevant to industrial applications and commercial devices.

In this study, electrodeposition was used to prepare porous Ni electrodes with high surface area values, ensuring that practical OER current densities could be reached at lower overpotential. To do so, we applied a Dynamic Hydrogen Bubbling Template (DHBT) method to prepare polycrystalline Ni electrodes with morphological features that facilitates the release

of oxygen bubbles during the OER. During the cathodic Ni deposition, hydrogen bubbles are concomitantly evolved due to the large cathodic potential applied. This leads to a nano-engineered electrode surface with an open porosity that reaches the underlying substrate. These deposits easily prepared using a fabrication process that could be scaled up. They are adherent, superaerophobic and mechanically stable under vigorous oxygen evolving conditions, and present very interesting OER properties

2. Experimental

2.1 Synthesis of porous Ni electrodeposits

Galvanostatic deposition (2 A cm^{-2}) from an aqueous solution of 0.1 M $NiCl_2 \cdot 6H_2O$ (ACROS Organics, ACS Reagent) and 2 M NH_4Cl (Fisher Chemical, Trace Metal Grade) was used to obtain fractal Ni foams with a honeycomb-like primary and cauliflower-like secondary structure. These electrodes will be denoted as Ni_{DHBT} (Dynamic Hydrogen Bubble Template) since both Ni deposition and H_2 evolution are occurring simultaneously. In all cases, commercial Ni plates (Alfa Aesar, Puratronic 99.9945% (metal basis)) were used as substrates. The films were deposited on one face of 1 cm x 1 cm Ni substrates. The electrodes were then sealed in bent glass tubes (90 degrees angle) so that the electrode surface was maintained in a vertical position and the Ni substrate uncovered face was not exposed to the electrolyte. In all cases, the exposed surface area was 1 cm^2. A saturated calomel electrode (SCE) and Pt gauze (Alfa Aesar, 99.9%) were used as reference and counter electrodes, respectively. For sake of clarity, all electrode potential values were converted to the Reversible Hydrogen Electrode (RHE) scale. The distance between the counter and the working electrode was fixed at *ca.* 5 mm. Ni electrodeposition was carried out using a Solartron 1480 A multipotentiostat for durations (T_d) up to 550 seconds. The faradaic efficiency for the Ni electroplating process was *ca.* 27 ± 8%, independently of the deposition duration. Following electroplating, the porous Ni electrodeposits were rinsed with water and dried under an Ar stream.

2.2 Physical characterization of porous Ni electrodeposits

The surface morphologies of porous Ni films were characterized by scanning electron microscopy (SEM) (JEOL, JSM-6300F) and thicknesses were measured by SEM cross-section analysis. Energy dispersive X-ray (EDX, VEGA3 TESCAN) measurements were performed to determine the Fe content. Contact angle measurements were performed as following. Images of water droplets and (captive) air bubbles in contact with the electrode surface were captured

by a Panasonic CCD camera (model GP-MF552). The volumes of the water droplet and air bubble were 5µL in both cases. Contact angles were calculated using ImageJ software with the Dropsnake plugin.

2.3 Electrochemical characterization and OER performances

Electrochemical characterization in Ar-saturated (Air Liquid, 99.999%) 1 M KOH (Fisher Chemical, ACS Reagent grade) was conducted in a conventional three-electrode system, using a Pt gauze and a saturated calomel electrode as auxiliary and reference electrodes, respectively. The working electrode and the counter electrode were not separated by a membrane. The solution (70 ml) was agitated by Ar bubbling. The distance between the working and the counter electrode was 5mm. Following a period of 10 minutes under open circuit potential (OCP) conditions, cyclic voltammograms (CV) (50 mV s^{-1}) with different potential windows (0.5V to 1.4 V, 0.5 V to 1.6 V, and 0.5 V to 1.9 V) were performed until steady-state potentiodynamic features were obtained. The last CV was recorded at 5 mV s^{-1}. Galvanostatic oxidation was carried out at 10 mA cm^{-2} for 15 min and then at 250 mA cm^{-2} for 15 min, followed by a last CV (0.5V to 1.9 V, 5 mV s^{-1}). This sequence was systematically applied to every Ni electrode studied in this work in order to ensure full conversion of nickel to β-$Ni(OH)_2$. The ohmic drop was measured by Electrochemical Impedance Spectroscopy (EIS) and an ohmic drop correction was manually applied to all potential values mentioned below.

In some cases, CVs and polarization curves were recorded in 1 M KOH electrolyte spiked with Fe. In those cases, the concentration of Fe was varied between 0 and 10 ppm through the addition of $FeCl_2 \cdot 6H_2O$ (Alfa Aesar, 98%).

EIS measurements in the OER potential range were obtained following 10 min polarization (from 1.44 to 1.49 V) between 0.01 Hz and 200 kHz using a FRA Analyser

(Solartron 1255B). Fitting to the de Levie equation was carried out by using Zview, with the de Levie element in series with the solution resistance and an inductor to model the typical wiring artifact seen at high frequencies. The values of R_{ct} and C_{dl} were derived from the fitted parameters, and so the software does not provide a standard error for them, but a naïve error propagation argument suggests that their standard errors are of the order of 5%.

Simulations of the transmission-line differential equations for porous electrodes [25-29] were performed by solving the ac and dc equations together as a system using Maple's default boundary value ODE solver, with an absolute error tolerance of 10^{-7} and a maximum number of mesh points of 256. For this purpose the two complex ac differential equations were converted to the four real differential equations below. The results were verified by comparing with those of Lasia [25,29] (who used a different method). The differential equations were scaled to represent the quantities on a geometric area basis (rather than for a single pore), in which they take the following form:

$$\frac{dE(X)}{dX} = -R_{\Omega}J(X);\ \frac{dJ(X)}{dX} = -j(E(X)) \qquad (1)$$

$$\text{with} \quad E(0) = E_0; J(1) = 0$$

$$\frac{d\tilde{E}(X)}{dX} = -R_{\Omega}\tilde{J}(X);\ \frac{d\tilde{J}(X)}{dX} = -\left(\mathrm{i}\omega C_{\mathrm{dl}} + \frac{dj(E(X))}{dE(X)}\right)\tilde{E}(X) \qquad (2)$$

$$\text{with} \quad \tilde{E}(0) = 1; \tilde{J}(1) = 0$$

Here X is the dimensionless distance into the pore, from 0 at the pore entrance to 1 at the pore base and $E(X)$ and $\tilde{E}(X)$ are the dc and ac (phasor) potentials down the pores. The quantities $J(X)$ and $\tilde{J}(X)$ are the dc and ac current densities (in solution) down the pores and R_{Ω} is the total solution resistance (Ω cm^2) within the pores, all with respect to geometric area and for the total number of pores in that area. The quantities C_{dl} (F cm^{-2}), and j (A cm^{-2}) are the local (specific) double-layer capacitance and current density on the pore walls, scaled by the roughness factor; the current density is assumed to have a Tafel potential dependence, as discussed below. The

potential at the pore entrance, E_0, is taken to be the experimental IR_s-corrected potential. The output is the predicted impedance $Z = \tilde{E}(0)/\tilde{J}(0) = 1/\tilde{J}(0)$.

3. Results and discussions

3.1 Morphology of Ni DHBT films

The morphological features of as-deposited Ni_{DHBT} films are shown in Figure 1. All electrodeposition parameters remained the same (-2 A cm^{-2} in 0.1 M $NiCl_2 \cdot 6H_2O$ + 2 M NH_4Cl) except for electrodeposition times (T_d). As seen in Figure 1A to 1D, increasing T_d led to a gradual increase of the Ni film thicknesses, from *ca.* 35 µm for T_d = 50 s up to 220 µm for T_d = 450 s. The deposited mass of Ni increased linearly up to 100 mg cm^{-2} for T_d = 450s (see Figure S1). The porosity of the films, calculated from the deposited mass and the measured thickness, varies between 30 and 50%. The mechanical stability of films deposited for longer duration (T_d = 550 s) is poor, with some parts detaching from the substrate upon rinsing, which causes the deposited mass to level off. The cross-section SEM micrographs of Figures 1A-1D also show that there are numerous voids along the observed dendritic structure of the films. Most of these voids are extending from the film surface to the underlying Ni plate substrate.

From top-view SEM micrographs (Figures 1E to 1 H), micrometer-sized pores are observed at the surface of the films, with pore diameter varying between 10 and 30 µm. Lower pore density and larger pore diameter are obtained for increased deposition times. This is typical of metal electrodeposition under vigorous hydrogen evolution (DHBT films). **Error! Bookmark not defined.**,30-41 In all cases, the pore walls exhibit a highly porous cauliflower-like secondary structure, with much smaller pore diameter (typically less than 500 nm). The structure seen in Figure 1 was observed over the entire 1 cm^2 geometric surface area of the deposits. It is expected that similar Ni structures could be formed on substrates with much larger geometric surface areas.

Contact angle measurements on captive air bubbles at the surface of Ni_{DHBT} films were performed and representative results are displayed in Figure 2. The contact angle of an air bubble increases from *ca.* 139° for Ni plate to *ca.* 160° for Ni_{DHBT} films, independently of the

DHBT deposition times. Enhanced air bubble contact angles were recently reported at laser-ablated Ni roughened plates (164°) as compared to Ni plates (126°).[42] Complementary water contact angle measurements were also performed to assess the hydrophilicity of Ni_{DHBT} films, essential for ensuring wetting of the porous structure of Ni_{DHBT} films and good contact of the latter with surface-active sites. To do so, sessile drop experiments were performed (5 µL of deionized H_2O) (see Figure 2). Ni_{DHBT} films presented superhydrophilic properties, with contact angles well below 25°, testament to the strong affinity of Ni_{DHBT} films toward water molecules. For the sake of comparison, Ahn *et al.* recently reported contact angle values of 30° and 42° for highly hydrophilic needle-like and cauliflower Ni electrodes, respectively. [43] In contrast, much larger contact angles (69°) were recorded on Ni plate, consistent with independent water contact angle studies on Ni plates (70 ± 3°). [42,43]

According to the Wenzel's model, the apparent contact angle on a rough surface, θ_r, is given by the following equation

$$\cos\theta_r = r\cos\theta \qquad with\cos\theta = \frac{\alpha_{13} - \alpha_{12}}{\alpha_{23}} \qquad (3)$$

where α_{12}, α_{13}, and α_{23} denote the interfacial tensions of the solid-liquid, the solid-gas, and the liquid-gas interface, respectively, r is the ratio of the true area of the solid surface to the apparent area, and θ is the Young contact angle as defined for an ideal surface of the same material. Because r is by definition greater than or equal to 1, Equation 3 predicts that roughness enhances the wetting/non-wetting intrinsic properties of any material, the extent of which is defined by the value of r.

An alternative way to deal with porous solid surfaces is to use equation (4) [44,45]

$$\cos\theta_f = \left(\frac{L}{l}\right)^{D-2}\cos\theta \qquad (4)$$

where L and l are the upper and lower limit lengths of fractal behavior, respectively, and D is the fractal dimension of the solid surface, with $2 \leq D \leq 3$. A fractal analysis based on the SEM cross-section image of the thicker Ni_{DHBT} film (T_d = 450 s) was conducted (see the supporting information section, Figure S2, for further details). The value of $(L/l)^{D-2}$ given by such calculation is 6.5. However, using the water contact angle of Ni plate as a reference, equation 4 predicts that $\cos\theta = 2.3$, which is obviously not possible. This discrepancy may be caused by air trapped beneath the water droplet. In these conditions, wetting follows the Cassie-Baxter wetting regime and Equation (4) can be re-written as Equation (5) [46]

$$\cos\theta_f = \left(\frac{L}{l}\right)^{D-2} f_s \cos\theta + f_s - 1 \qquad (5)$$

with f_s being the fraction of the surface that is wetted by water. So, assuming that f_s=0.6 (the water droplet is wetting 60% of the Ni_{DHBT} film underneath), the contact angle measurements are in agreement with the fractal analysis. The use of Equation 5 implies that Ni_{DHBT} films should be treated like porous materials and that partial spontaneous invasion of liquid inside the texture of these films is taking place through capillary action. Further decrease of θ_f could be achieved by increasing $(L/l)^{D-2}$ and/or f_s . This could be achieved through modification of the Ni_{DHBT} deposition conditions. Also, it should be noted that the above discussion on the wetting property is based on the *ex-situ* contact angle observations. It reflects the hydrophilic properties of Ni_{DHBT} film, but the air entrapment assumption used in equation 5 would not necessarily be valid in the real gas evolution situations. So, future *in-situ* observations on the contact angle measurement should be made to evaluate the full benefits of Ni_{DHBT} films in releasing the bubbles, but this is however outside of the scope of the present study.

3.2 Electrochemical characterization

The electrochemical properties of porous Ni_{DHBT} coatings were first determined through CV measurements. Following repetitive potential cycles (see the experimental section for

details) until the formation of a hydrous Ni oxide deposit was achieved, [47] steady-state CV profiles were obtained and are shown in Figure 3. All Ni_{DHBT} CVs exhibit a large oxidation (at *ca.* 1.41 V) and reduction peak (at *ca.* 1.28 V), whose intensities grow with the film thicknesses. The assignment of these peaks will be discussed later. For each Ni_{DHBT} electrode, the ratio between the anodic (Q_a) and the cathodic (Q_c) coulombic charge of this redox transition remained similar, with a mean value of *ca.* 1.00 ± 0.13. Q_a values were found to increase continuously from 62 ± 4 mC cm^{-2} for T_d = 50s to 539 ± 57 mC cm^{-2} for T_d = 450s (Figure S3). These values correspond to electrochemically active surface enhancement factors of *ca.* 30 and 270, respectively, considering the Q_a value of a commercial Ni plate as a reference (2.1 ± 0.1 mC cm^{-2}). Once normalized to the deposited mass, *m*, (Figure S3), the ratio Q_a/m is remarkably constant. This is a clear indication that the material deposited at the beginning of the deposition period is not occluded by that deposited at the end of the deposition process. This is consistent with the presence of numerous small (< 500 nm) and large (10 – 30 μm) pores seen in Figure 1. For comparison, there is a factor of *ca*. 25 increase between the Q_a values of Ni foams and Ni_{DHBT} films (Figure S4). The good mechanical stability, highly porous structure and tremendous capacity of Ni_{DHBT} films to store charge makes it an attractive material and/or substrate for low-cost pseudo supercapacitor devices, as charge density values in excess of 500 mC cm^{-2} observed for Ni_{DHBT} of 450 s are well above those reported recently for hierarchical porous Ni/NiO electrodes. [48] Higher electrochemically active surface areas were obtained for Ni_{DHBT} of 550 s (660 mC cm^{-2}); however, these later films have mechanical stability issues (some part of the deposits might detached from the substrate), causing a large dispersion in the data (see the error bar in Figure S3). In the future, a subsequent heat-treatment might help improve the mechanical stability of the thickest films through sintering of Ni grains, therefore allowing the preparation of adherent films with larger electrochemically active surface areas.

In this work however, no such heat-treatment was applied and this aspect will be investigated in an upcoming study.

On the thinnest Ni_{DHBT} films (T_d = 50 s), the main oxidation peak is centered at *ca.* 1.39 V. It corresponds to the well-known α-$Ni(OH)_2$/γ-NiOOH transition.[47,49] There is also a shoulder at *ca.* 1.43V, which is attributed to β-$Ni(OH)_2$/β-NiOOH transition. Both contributions are always observed as the Ni_{DHBT} film thickens (Figure S5), but the relative intensity of the β-$Ni(OH)_2$/β-NiOOH transition increases steadily from the thinnest to the thicker films, as can be assessed from the relative intensity at 1.39 and 1.43 V. The position and the relative intensity of both transitions do not vary with the scan rate (not shown). However, for the moment, we do not have an explanation to understand why the ratio between these two components vary with the film thicknesses.

All Ni_{DHBT} films exhibit an additional oxidation wave at *ca.* 1.56 V, whose intensity increases with thickness. This oxidation wave is attributed to formation of Ni (IV) species, potentially at the edges of γ-$Ni(OH)_2$/γ-NiOOH domains. [49,50] At more positive potentials ($E \geq$ 1.60 V), O_2 evolution occurred with high current densities, which systematically increased upon increasing Ni_{DHBT} film thickness. For Ni_{DHBT} films of 50 s and 450 s, current density values of *ca.* 25 mA cm^{-2} were obtained at 1.72 V and 1.64 V, respectively. Conversely, at 1.64 V, the OER current density increased by a factor of five, from 5 mA cm^{-2} to 25 mA cm^{-2}, upon increasing Ni_{DHBT} deposition times from 50s to 450s.

Galvanostatic experiments (250 mA cm^{-2}) were performed on Ni_{DHBT} electrodes in 1 M KOH. The corresponding results are presented in Figure 4A. Stable potentials were obtained for Ni_{DHBT} electrodes right from the beginning of experiments. In contrast, a gradual increase of the potential was observed for bare Ni plates during the first 10 minutes of electrolysis. For longer electrolysis periods, the OER potential of Ni plates stabilized at 2.05 V. It should be

noted that the electrochemical behaviors presented in Figure 4A were reproducibly obtained

for a minimum of three different Ni electrodes (see Figure S6). In Figure 4B, the *iR*-corrected overpotentials reached after 15 minutes of electrolysis at +250 mA cm^{-2}, $\eta_{250,}$ are plotted with respect to the deposition time. There is *ca* 300 mV difference between η_{250} of Ni plate and the best performing Ni_{DHBT} films. As shown previously, Q_a is directly proportional to the deposition time (Figure S3) and can be used as an indirect measure of the electrochemically active surface area. Figure S7 shows that E_{250} values of Ni_{DHBT} films scales linearly with Q_a plotted on a semi-logarithmic scale, which is the behavior expected if all the material making up the Ni_{DHBT} films is involved in the OER. This suggests that, even at high current density (250 mA cm^{-2}) and for the thicker films, the electrolyte has access to the whole porous structure and that the O_2 bubbles do not lead to a decrease of the available Ni catalytic sites.

According to the seminal work of Boettcher[49] and Corrigan[51], the observation of a redox transition at 1.56 V before the onset for the OER in Figure 3 is a clear signature of $Ni(OH)_2$ aged or cycled in a rigorously Fe-free electrolyte. In contrast, the same studies indicate that cycling or aging of $Ni(OH)_2$ in Fe-contaminated KOH solution, even at the ppm level, leads to a huge improvement of the activity for the OER. Accordingly, potential cycling of Ni_{DHBT} electrodes 1 M KOH electrolyte spiked with 10 ppm of $FeCl_2$ was performed. As seen in Figure 5A, the onset potential for the OER is shifted negatively by at least 100 mV in presence of Fe impurities, pointing toward a reduction of the energy barriers of some of the intermediates in the OER process. This occurs even if the charge under the redox peaks centered at *ca* 1.39 V is hardly changed (although the shape of the oxidation and reduction peaks are slightly modified), suggesting the surface density of active sites was not changed. The Fe content of these electrodes remains low (0.6%, as determined by EDX analysis). Galvanostatic curves (j = 250 mA cm^{-2}) recorded in 1 M KOH spiked with 10 ppm $FeCl_2$ are shown in Figure 5B. These potential *vs* time curves are as stable as they are in the absence of Fe impurities. The two sets of SEM micrographs taken before and after electrolysis are virtually undistinguishable

from one another (Figure S8), indicating that the electrode structure is morphologically stable even under vigorous O_2 evolution. This is consistent with the CVs of electrodes taken at the beginning and the end of the polarization period being almost superimposed on each other (Figure S9).

Figure 5C shows the steady-state *iR*-corrected potential *vs* log(*j*) curves (Tafel plot) on both Ni plate and the best performing Ni_{DHBT} electrode (T_d = 450 s) with 10 ppm $FeCl_2$ in the electrolyte. The Tafel slopes are 31 and 29 mV/dec for Ni plate and Ni_{DHBT}, respectively, which indicates that the mechanisms responsible for the OER are the same on both electrodes. Even if the Ni_{DHBT} films have an EASA that is 270× larger than a Ni plate, Fe impurities are interacting with the Ni sites at this extended surface in the same way they are with Ni sites distributed on a flat surface. Part of the reason for this behavior might be related to the open structure of Ni_{DHBT} films that is not hampering the diffusion of Fe impurities through the film and their interaction with Ni sites. This assertion is supported by the results of Figure S3, showing that the coulombic charge, Q_a, of the redox transition at *ca* 1.41 V scales linearly with T_d (and thus the mass of the film). The data of Figure 5C also shows that, in the "Tafel region", there is a factor *ca* 230x difference of the (apparent) current density between both substrates, very close from the 270x increase of the EASA determined previously. This means that almost all the extended surface area of Ni_{DHBT} films have been modified by Fe impurities and is active for the OER.

In order to clearly correlate the enhanced OER property to the 3D structure of Ni_{DHBT} films, a series of EIS measurements was performed. The impedance spectra of Figure 6 shows the classic features associated with porous electrodes: a small potential-independent feature at high frequencies whose shape is dependent on pore geometry but is a 45^0 line for pores of uniform cross section, and a low-frequency semicircle reflecting the reaction on the pore walls,

with a potential-dependent diameter that is the charge-transfer resistance. The de Levie

impedance, Equation (6),[52] in series with the solution resistance and an inductor (not shown) to describe high-frequency wiring artifacts gave excellent fits to the data (Figure 6).

$$Z_{pore} = \frac{R_\Omega}{\Lambda^{1/2}} \coth\left(\Lambda^{1/2}\right) \quad \text{with} \quad \Lambda = i\omega c_{dl} + 1/r_{ct} \qquad (6)$$

The parameters c_{dl} and r_{ct} are the double-layer capacitance and charge-transfer resistance on the pore walls combined with some geometric factors. The equation is usually written for a single cylindrical pore, but scaling by the geometric area per pore gives the experimental impedance for all the pores on a geometric area basis. In this case, the total pore wall capacitance and total charge-transfer resistance, which is related to the local pore wall values through the roughness factor, may be extracted from the fitted parameters by

$$C_{\mathrm{dl}} = c_{dl} / R_\Omega$$

$$R_{\mathrm{ct}} = r_{\mathrm{ct}} R_\Omega$$

Values for these parameters are shown in Table 1. The capacitance and charge-transfer resistance values obtained in this way were not significantly different from those found by fitting only the low-frequency semicircle to a parallel C_{dl}-R_{ct} circuit. This is expected since for small values of x, $\coth(x^{1/2})/x^{1/2} \approx x^{-1}$ and $Z_{\mathrm{pore}} \approx \left(i\omega C_{\mathrm{dl}} + 1/R_{\mathrm{ct}}\right)^{-1}$.

Although the theory is usually written in terms of cylindrical pores, it is easily extended to arrays of pores with uniform cross section down the pore [53,54], and geometry enters only through the total wall area per geometric area. The same equation has also been derived from a macrohomogeneous model by Paasch et al [55], where the pore geometry is arbitrary but with features small compared to the depth of the porous structure. Candy et al[56] showed experimentally that the impedance is insensitive to the pore geometry, and that a pore of stacked spheres gave similar results to cylindrical pores. So the fact that the measured impedance here closely fits the de Levie equation despite the complex geometry is not surprising.

There are some geometric factors that do lead to departure from this equation. A distribution of pore sizes of the same geometry gives similar results at high frequencies, but a new frequency dispersion arises at low frequencies. [57,58] On the other hand, non-uniform pores, with significantly different cross sectional areas going down the pore, affect the shape of the high-frequency part of the pore impedance.[59] Neither of these features are seen here. Secondary pores off the primary pore, or fractal structures show linear behavior at high frequencies, but with angles much less than 45°. [60,61] Although the structures here are fractal, this is not reflected in the impedance, perhaps because secondary pores are inactive, which is in line with the value of $f_s = 0.6$ determined previously from the analysis of the contact angle data, or the behaviour is dominated by pores with larger cross sections.

Although the de Levie/Paasch derivations of Eq. (1) assume uniform structures, they neglect the fact that the local interfacial current density going down the pore will not be uniform because the solution potential and hence the local overpotential is changing down the pore. Lasia [26] numerically solved the transmission line differential equations to allow for a change in local overpotential and showed that the discrepancy between the fitted and local charge transfer resistance can be as high as a factor of two. Accordingly we sought to correct for this factor. Lasia divided the pores into small sections and used an integration method, and Nguyen and Paasch [62] likewise divided the pore into small sections and used a transfer matrix method. However, here we used a standard differential equation solver, which automatically adjusts the mesh size down the pore to give the required accuracy (see Methods section). Initially we used the fitted R_{ct} and C_{dl} values, and assumed that the local current-potential relationship within the pores was the same as the Tafel slope measured at that dc potential. Taking the 1.47 V data as an example (Figure 7), the predicted impedance is too high (blue curve), with the (iR-corrected) low-frequency intercept 15% higher than the experimental values, suggesting the real current-potential relationship within the pores has a 15% lower Tafel slope. Making this change, and

leaving the other parameters (R_Ω and C_{dl}) constant, gives excellent agreement with the experimental data, both in the Nyquist plot (red curve) and Bode plot (not shown). The simulations show that the reason is that the change in overpotential going down the pore is 1.5 mV. While this seems small, the steep current-potential (Tafel) relationship means that this amounts to a significant change in current density, and consequently the measured impedance is significantly affected. The effect is less noticeable on the actual Tafel plots, predicting only a 4 mV/dec change from a smooth surface to the porous material, which is within the variation from sample to sample.

In recent years, activities for the OER were judged by the potential required to oxidize water at a current density of 10 mA cm^{-2}, a metric relevant to solar fuel synthesis.[63] As shown in Figure 5C, the overpotential at 10 mA cm^{-2}, η_{10}, of the best Ni_{DHBT} film is 250 mV, which is 70 mV lower than the best performing materials reported in that study that review some of the most promising electrode materials. For applications in electrolyzers, comparison at much larger current density must be made. In presence of 10 ppm $FeCl_2$, η_{250} values as small as 310 mV were reached for the Ni_{DHBT} electrode with T_d = 450 s. In comparison, Guo and Li recently reported an OER overpotential at 100 mA cm^{-2}, η_{100}, of 312 mV in 1M KOH for iron-doped nickel hydroxide prepared at room temperature on Ni foam,[64] which is already better than those reported in previous works. [65,66] However, from the data of Figure 5C, this is still 32 mV larger than the overpotential recorded on Ni_{DHBT} at the same current density. Elsewhere, FeCoNi deposited on Ni foam were shown to deliver 75 mA cm^{-2} at an overpotential of 320 mV in 1 M KOH, [67] which is 44 mV larger than at Ni_{DHBT} films (η_{75} = 276 mV from Figure 5C).

There are several reasons that can explain the performances of Ni_{DHBT} films. There is no doubt that the increased electrochemically active surface area of Ni_{DHBT} films, as compared to Ni plates, is in part responsible for the improved OER performance. As stated previously

(Figure S7), the electrochemically active surface area of Ni_{DHBT} films is fully accessible to the

electrolyte and participates in the O_2 evolution reaction. However, this measure of the active area was performed in a potential region where no gas evolution is occurring. Owing to the porous structure of Ni_{DHBT} films, one could have expected that, at more positive potential in the OER region, O_2 bubbles could increase the electrolyte resistance and/or be responsible for occlusion of some of the pores. However, this is not what is observed, and the EIS data of Table 1 shows that the double layer capacitance is constant in the potential region where the 29 mV /decade Tafel slope is observed. This indicates that occlusion of Ni active sites by O_2 bubbles is not a limiting factor.

It is undeniable that the low Tafel slope (29 mV/decade) is a major factor contributing to the performance of the Ni_{DHBT} films. On Ni_{DHBT} films, the 29 mV/decade Tafel slope is observed over a range of current densities that far exceed that of Ni plate. Indeed, the "low Tafel slope region" extends up to 100 mA cm^{-2} on Ni_{DHBT} films while it is limited to 5 mA cm^{-2} on Ni plate. This striking difference is partly responsible for the increased performance of the Ni_{DHBT} films and must be related to their different morphologies.

As described in the introduction, recent reports have shown that the morphology of the electrodes has an impact on the adhesion force of gas bubbles to the surface and the detachment diameter of the same gas bubbles upon release. Indeed, both the adhesion force and the detachment diameter of gas bubbles are diminished through nanostructuring of the electrode surface.[12,18] According to what is referred to in the literature as the Fritz correlation, there is a linear relationship between the gas bubble detachment diameter from a surface and its water contact angle. [68] As mentioned earlier, the water contact angle decreases from 60° to less than 25° as a result of the fractal geometry of the Ni_{DHBT} electrode. Enhanced air bubble contact angle, which is a direct consequence of increased hydrophilicity, translates into smaller bubble adhesive forces on the electrode surface (and smaller residency time), along with smaller radius of the contact plane between air bubble and the electrode surface (and thus larger contact area

between the electrolyte and the electrode active sites). The significant decrease of the adhesion force and detachment diameter of gas bubbles resulting from nanostructuring of the electrode will need to be confirmed by independent measurements but this could also help understand the morphological stability of Ni_{DHBT} films under vigorous oxygen evolving conditions.

We have succeeded in developing a robust and mechanically stable electrode made of a cheap and sustainable material. These Ni_{DHBT} films are wetted by the electrolyte (f_s = 0.6), translating in very large electrochemically active surface area. They also exhibit a superaerophobic character responsible for small air bubble contact angle and small air bubble adhesive force, both factors further contributing to maximize the surface area contact between the active sites of the electrolyte and the electrolyte even in conditions where strong O_2 evolution is occurring. This translates into a small overpotential even in conditions where vigorous oxygen evolution is occurring. On this matter, it is worth remembering that Ni_{DHBT} films are prepared by electrodeposition in conditions where hydrogen evolution occurs concomitantly with Ni metal deposition. As mentioned earlier, the faradaic efficiency for Ni deposition is close to 30%, which means that a large fraction of the current is used to generate hydrogen gas that escapes the electrode in the form of gas bubbles. The implication of this is that, *right from their formation, Ni_{DHBT} films are templated in such a way that gas bubbles can freely escape the growing film without causing any damage to its structure*. The existence of several paths through which gas bubbles can escape without causing damage to the film might also have proven to be a critical factor in the stability of the Ni_{DHBT} films. From a broader viewpoint, such *gas bubble-architectured* materials represent an attractive design of active and stable catalysts for other gas evolving electrochemical reactions.

4. Conclusions

It was shown that dynamic hydrogen bubble templating could be used to prepare Ni_{DHBT} films with a fractal structure, which exhibit improved OER properties compared to Ni plate. The best performing Ni_{DHBT} films are highly porous and have an electrochemically accessible surface area increased by a factor of 270 as compared to the underlying Ni plate. They are mechanically robust and do not degrade under vigorous oxygen evolution. In presence of 10 ppm $FeCl_2$, OER overpotential at 250 mA cm^{-2} is only 310 mV. This is due to both the porous nature of the deposit and the superaerophobic nature of the fractal Ni films, which leads to an increase of the contact angle of a trapped air bubble and a significant decrease of the adhesion force of O_2 gas bubbles. Industrial applications of these Ni_{DHBT} templates could be envisioned depending on the availability of suitable pieces of equipment for dynamic hydrogen bubble templating on substrates with larger geometrical surface area. Investigations are planned for scaling the additive manufacturing of fractal Ni-based coatings for use in advanced electrolysis cell configurations, to further examine transport enhancement in relevant industrial systems and its tolerance to commercially relevant alkaline solutions.

ACKNOWLEDGEMENTS

This research was conducted as part of the Engineered Nickel Catalysts for Electrochemical Clean Energy project administered from Queen's University and supported by Grant No. RGPNM 477963-2015 under the Natural Sciences and Engineering Research Council of Canada (NSERC) Discovery Frontiers Program. One of us (V. C.) would also like to acknowledge the Natural Sciences and Engineering Research Council (NSERC) for an Undergraduate Research Award.

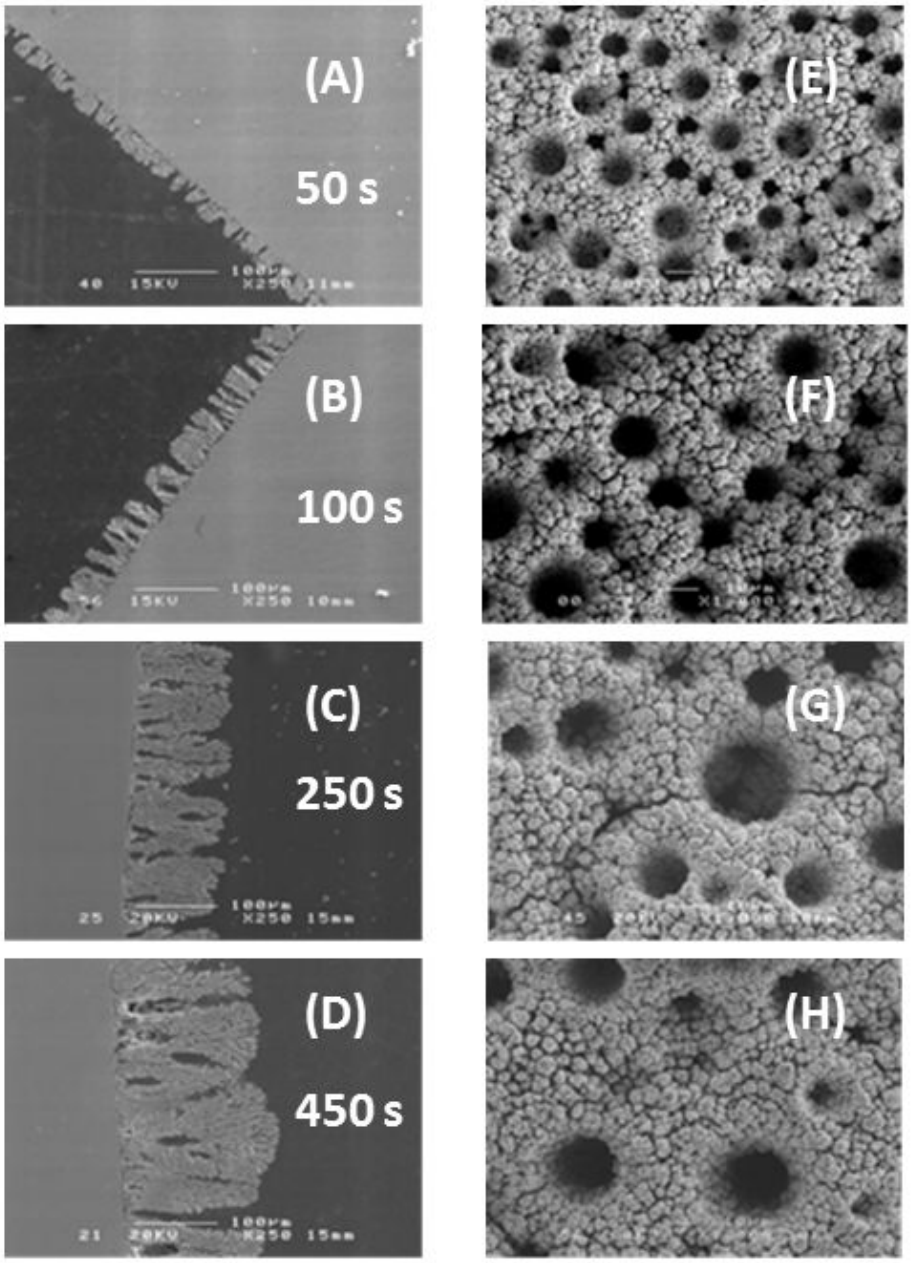

Figure 1 Effect of electrodeposition time (values inserted for each sample) on the morphological features of Ni_{DHBT}. The deposition conditions are the following: -2 A cm^{-2} in 0.1 M $NiCl_2 \cdot 6H_2O$ + 2 M NH_4Cl; cross-section (A-D) and corresponding top-view images (E-H).

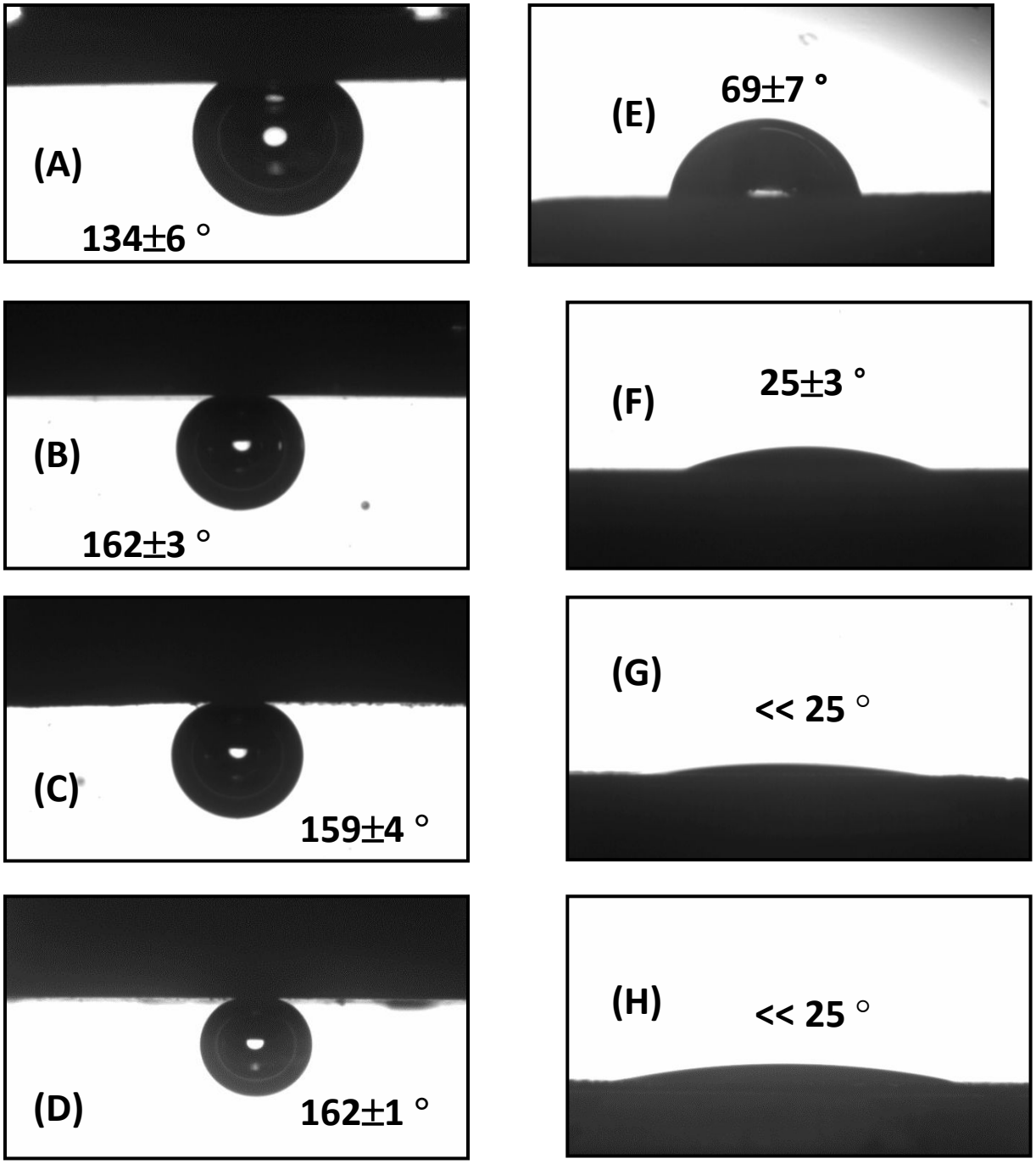

Figure 2 Contact angle images for a 5 µL air bubble (A-D) and a 5 µL water droplet (E-H) on Ni plate (A, E); Ni_{DHBT} with T_d = 50s (B, F); Ni_{DHBT} with T_d = 250s (C, G); and Ni_{DHBT} with T_d = 450s (D, H).

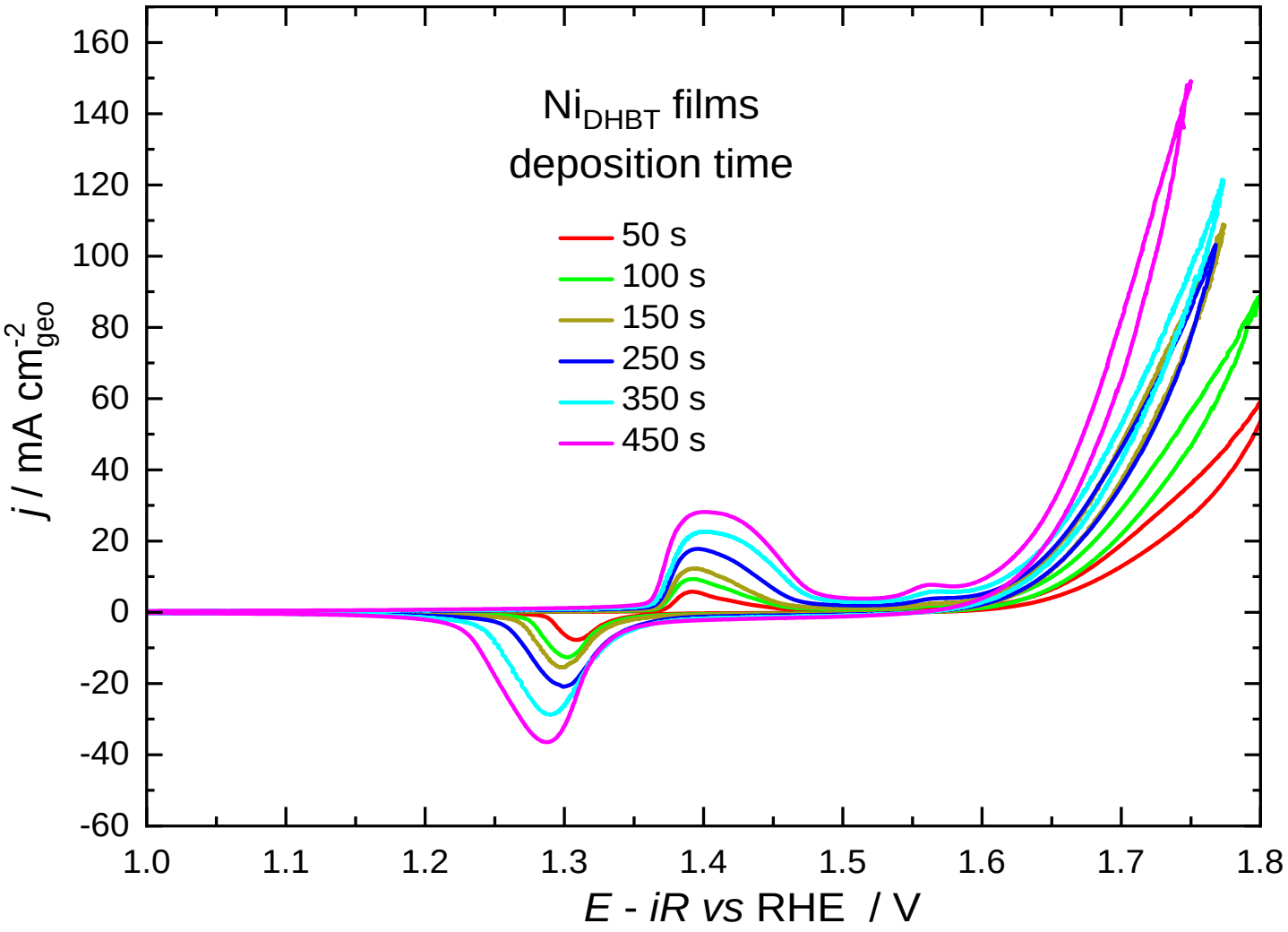

Figure 3 Cyclic voltammograms (5 mV s^{-1}) in 1 M KOH for Ni electrodes obtained through the Dynamic Hydrogen Bubble Template electrodeposition method. The electrodeposition time is shown for each electrode.

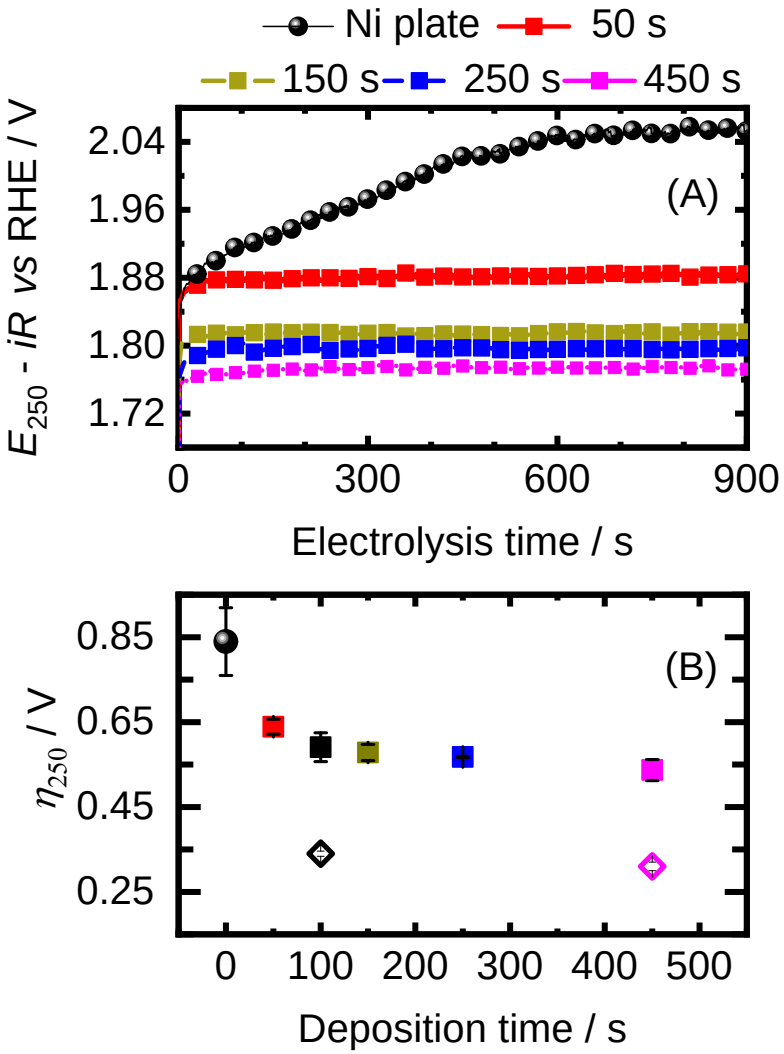

Figure 4 In (A), chronopotentiometric curves at +250 mA cm^{-2} in 1 M KOH for Ni_{DHBT} electrodes prepared at different electrodeposition times. In (B), corresponding potential values recorded at t = 900 s. The error bars were obtained from three independent measurements performed on a set of three electrodes prepared in the same conditions (three replicates, see Figure S6). The open symbols (◊) are for Ni_{DHBT} electrodes measured in 1 M KOH spiked with 10 ppm of Fe impurities.

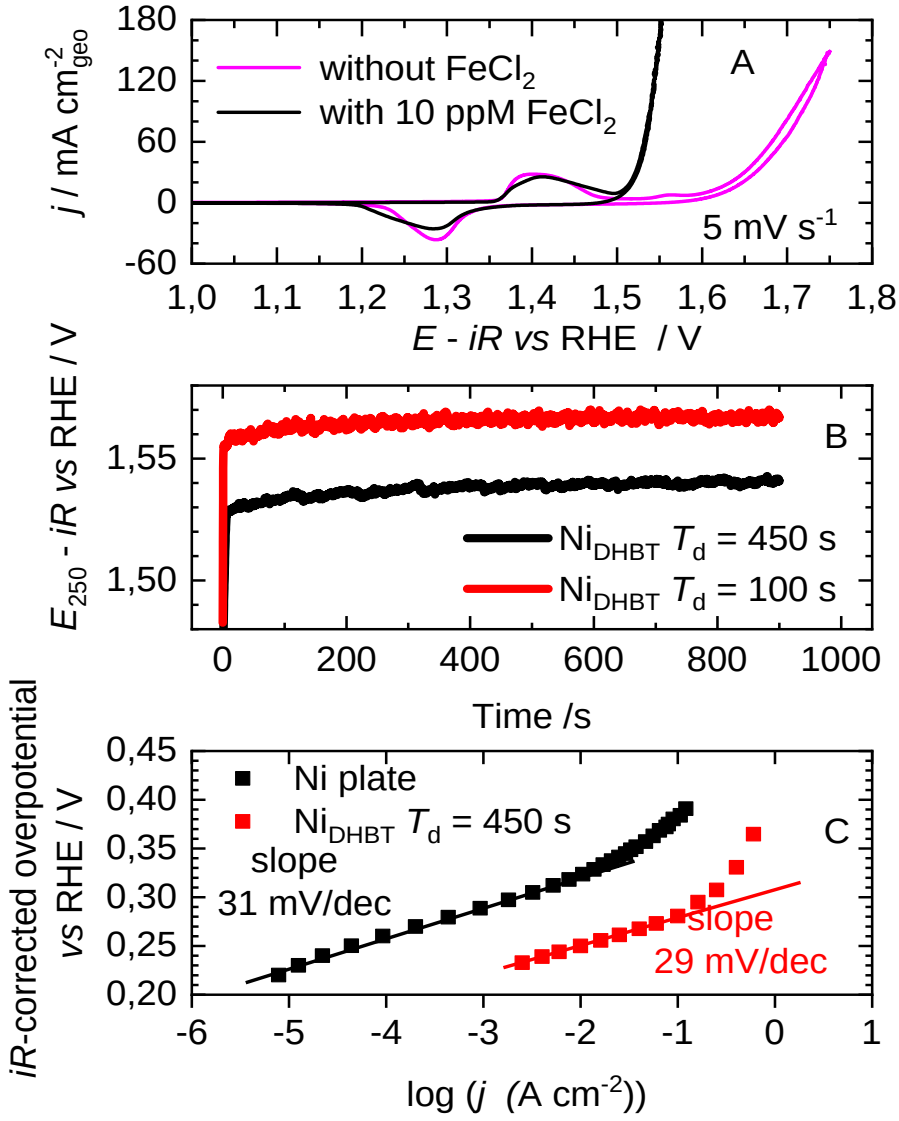

Figure 5 In (A), effect of the presence of $FeCl_2$ (10 ppm) on the CVs of Ni_{DHBT} film. In (B), chronopotentiometric curves recorded at +250 mA cm^{-2} in 1 M KOH spiked with $FeCl_2$ (10 ppm). In (C), variation of the *iR*-corrected overpotential *vs* the logarithm of the steady-state current density, *j*. The electrolyte was 1 M KOH spiked with 10 ppm $FeCl_2$. The Tafel slopes are 31 and 29 mV/dec for Ni plate and Ni_{DHBT} film, respectively.

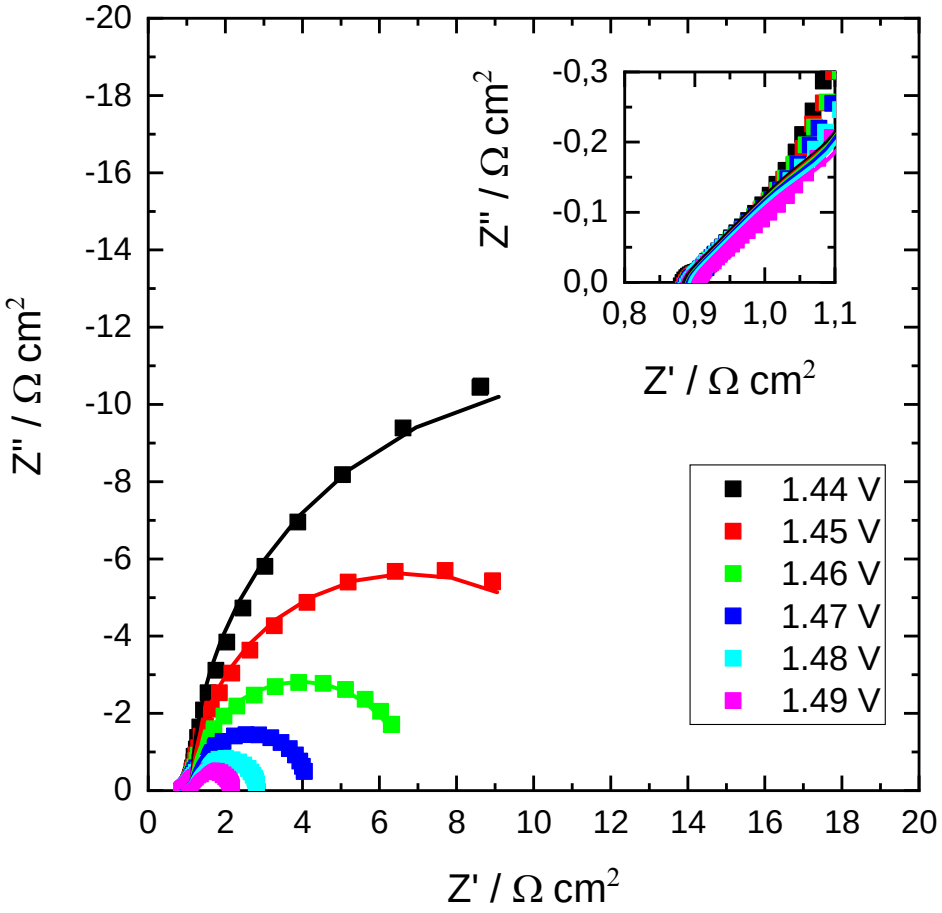

Figure 6 Measured (scattered points) and fitted (solid lines) EIS plots on a Ni_{DHBT} film (T_d = 450 s) at different potentials. The electrolyte was 1M KOH spiked with 10 ppm $FeCl_2$. The high-frequency features are shown in the insert.

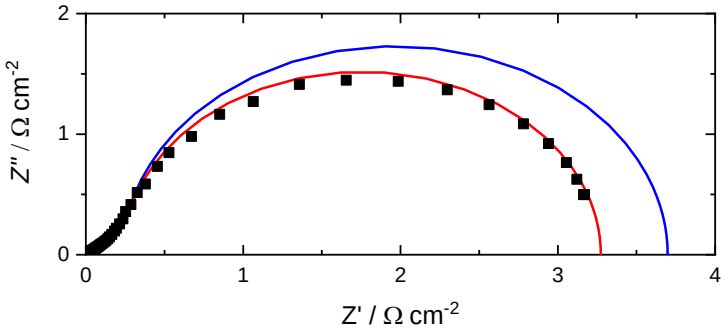

Figure 7 Measured EIS plot (scatter points) on a Fe-modified Ni_{DHBT} film (T_d = 450 s) at potential 1.47V vs RHE. Solid lines are simulation results of solving Eqs. (1) and (2). The blue line assumes the measured Tafel slope at 1.47 V (31 mV/dec) is valid also within the pores; the red line assumes an adjusted relationship (27 mV/dec) applies within the pores.

Table 1: Parameters from EIS fits. The sample was Ni_{DHBT} (T_d = 450 s) and the electrolyte was 1 M KOH at room temperature spiked with 10 ppm $FeCl_2$.

iR-corrected potential *vs* RHE (V)	R_s (Ω cm^2)	c_{dl} (s)	R_Ω (Ω cm^2)	r_{ct}	R_{ct} (Ω cm^2)	C_{dl} (F cm^{-2})
1,439	0.88	0.78	0.81	26.07	21.04	0.97
1,449	0.88	0.75	0.82	13.78	11.24	0.92
1,458	0.88	0.69	0.78	7.24	5.64	0.88
1,466	0.88	0.65	0.75	3.95	2.97	0.87
1.473	0.88	0.64	0.73	2.30	1.68	0.87
1.479	0.89	0.64	0.71	1.46	1.04	0.91

REFERENCES

1 Suen, N.-T.; Hung, S.-F.; Quan, Q.; Zhang, N.; Xu, Y.-J.; Ming Chen, H. Electrocatalysis for the Oxygen Evolution Reaction: Recent Development and Future Perspectives. *Chem. Soc. Rev.* **2017**, 46 (2), 337–365.

2 Cheng, Y.; Jiang, S. P. Advances in Electrocatalysts for Oxygen Evolution Reaction of Water Electrolysis-from Metal Oxides to Carbon Nanotubes. *Prog. Nat. Sci.: Mater. Int.* **2015**, 25 (6), 545–553.

3 Suntivich, J.; May, K. J.; Gasteiger, H. A.; Goodenough, J. B.; Shao-Horn, Y. A Perovskite Oxide Optimized for Oxygen Evolution Catalysis from Molecular Orbital Principles. *Science* **2011**, 334 (6061), 1383–1385.

4 Li, M.; Xiong, Y.; Liu, X.; Bo, X.; Zhang, Y.; Han, C.; Guo, L. Facile Synthesis of Electrospun MFe2O4 (M = Co, Ni, Cu, Mn) Spinel Nanofibers with Excellent Electrocatalytic Properties for Oxygen Evolution and Hydrogen Peroxide Reduction. *Nanoscale* **2015**, 7 (19), 8920–8930.

5 Kang, Q.; Vernisse, L.; Remsing, R. C.; Thenuwara, A. C.; Shumlas, S. L.; McKendry, I. G.; Klein, M. L.; Borguet, E.; Zdilla, M. J.; Strongin, D. R. Effect of Interlayer Spacing on the Activity of Layered Manganese Oxide Bilayer Catalysts for the Oxygen Evolution Reaction. *J. Am. Chem. Soc.* **2017**, 139 (5), 1863–1870.

6 Diaz-Morales, O.; Ferrus-Suspedra, D.; Koper, M. T. M. The Importance of Nickel Oxyhydroxide Deprotonation on Its Activity towards Electrochemical Water Oxidation. *Chem. Sci.* **2016**, 7 (4), 2639–2645.

7 Zeng, K.; Zhang, D. Recent Progress in Alkaline Water Electrolysis for Hydrogen Production and Applications. *Prog. Energy Combust. Sci.* **2010**, 36 (3), 307–326.

8 Cheng, H.; Scott, K.; Ramshaw, C. Intensification of Water Electrolysis in a Centrifugal Field. *J. Electrochem. Soc.* **2002**, 149 (11), D172–D177.

9 Wang, M.; Wang, Z.; Guo, Z. Understanding of the Intensified Effect of Super Gravity on Hydrogen Evolution Reaction. *Int. J. Hydrogen Energy* **2009**, 34 (13), 5311–5317.

10 Wang, M.; Wang, Z.; Guo, Z. Water Electrolysis Enhanced by Super Gravity Field for Hydrogen Production. *Int. J. Hydrogen Energy* **2010**, 35 (8), 3198–3205.

11 Li, S.-D.; Wang, C.-C.; Chen, C.-Y. Water Electrolysis in the Presence of an Ultrasonic Field. *Electrochim. Acta* **2009**, 54 (15), 3877–3883.

12 Lu, Z.; Li, Y.; Lei, X.; Liu, J.; Sun, X. Nanoarray Based "Superaerophobic" Surfaces for Gas Evolution Reaction Electrodes. *Mater. Horiz.* **2015**, 2 (3), 294–298.

13 Li, Y.; Hasin, P.; Wu, Y. NixCo3−XO4 Nanowire Arrays for Electrocatalytic Oxygen Evolution. *Adv. Mater.* **2010**, 22 (17), 1926–1929.

14 Lu, B.; Cao, D.; Wang, P.; Wang, G.; Gao, Y. Oxygen Evolution Reaction on Ni-Substituted Co3O4 Nanowire Array Electrodes. *Int. J. Hydrogen Energy* **2011**, 36 (1), 72–78.

15 Lu, Z.; Xu, W.; Zhu, W.; Yang, Q.; Lei, X.; Liu, J.; Li, Y.; Sun, X.; Duan, X. Three-Dimensional NiFe Layered Double Hydroxide Film for High-Efficiency Oxygen Evolution Reaction. *Chem. Commun.* **2014**, 50 (49), 6479–6482.

16 Liu, X.; Chang, Z.; Luo, L.; Xu, T.; Lei, X.; Liu, J.; Sun, X. Hierarchical ZnxCo3–XO4 Nanoarrays with High Activity for Electrocatalytic Oxygen Evolution. *Chem. Mater.* **2014**, 26 (5), 1889–1895.

17 Yang, Q.; Li, T.; Lu, Z.; Sun, X.; Liu, J. Hierarchical Construction of an Ultrathin Layered Double Hydroxide Nanoarray for Highly-Efficient Oxygen Evolution Reaction. *Nanoscale* **2014**, 6 (20), 11789–11794.

18 Lu, Z.; Zhu, W.; Yu, X.; Zhang, H.; Li, Y.; Sun, X.; Wang, X.; Wang, H.; Wang, J.; Luo, J.; Lei, X; Jiang, L. Ultrahigh Hydrogen Evolution Performance of Under-Water "Superaerophobic" MoS_2 Nanostructured Electrodes. *Adv. Mater.* **2014**, 26 (17), 2683–2687.

19 Kong, D.; Wang, H.; Lu, Z.; Cui, Y. CoSe2 Nanoparticles Grown on Carbon Fiber Paper: An Efficient and Stable Electrocatalyst for Hydrogen Evolution Reaction. *J. Am. Chem. Soc.* **2014**, 136 (13), 4897–4900.

20 Faber, M. S.; Dziedzic, R.; Lukowski, M. A.; Kaiser, N. S.; Ding, Q.; Jin, S. High-Performance Electrocatalysis Using Metallic Cobalt Pyrite (CoS_2) Micro- and Nanostructures. *J. Am. Chem. Soc.* **2014**, 136 (28), 10053–10061.

21 Nam, D. H.; Kim, R. H.; Han, D. W.; Kwon, H. S. Electrochemical Performances of Sn Anode Electrodeposited on Porous Cu Foam for Li-Ion Batteries. *Electrochim. Acta* **2012**, 66, 126–132.

22 Jeong, M.-G.; Zhuo, K.; Cherevko, S.; Kim, W.-J.; Chung, C.-H. Facile Preparation of Three-Dimensional Porous Hydrous Ruthenium Oxide Electrode for Supercapacitors. *J. Power Sources* **2013**, 244, 806–811.

23 Niu, X.; Zhao, H.; Chen, C.; Lan, M. Enhancing the Electrocatalytic Activity of Pt–Pd Catalysts by Introducing Porous Architectures. *ChemCatChem* **2013**, 5 (6), 1416–1425.

24 Wang, Y.; Arandiyan, H.; Scott, J.; Bagheri, A.; Dai, H.; Amal, R. Recent Advances in Ordered Meso/Macroporous Metal Oxides for Heterogeneous Catalysis: A Review. *J. Mater. Chem. A* **2017**, 5 (19), 8825–8846.

25 Los, P.; Lasia, A.; Ménard, H.; Brossard, L. Impedance Studies of Porous Lanthanum-Phosphate-Bonded Nickel Electrodes in Concentrated Sodium Hydroxide Solution. *J. Electroanal. Chem.* **1993**, 360 (1), 101–118.

26 Lasia, A. Impedance of Porous Electrodes. *J. Electroanal. Chem.* **1995**, 397 (1), 27–33.

27 Shervedani, R. K.; Lasia, A. Kinetics of Hydrogen Evolution Reaction on Nickel-Zinc-Phosphorous Electrodes. *J. Electrochem. Soc.* **1997**, 144 (8), 2652–2657.

28 Hitz, C.; Lasia, A. Experimental Study and Modeling of Impedance of the Her on Porous Ni Electrodes. *J. Electroanal. Chem.* **2001**, 500 (1), 213–222.

29 Lasia, A. Nature of the Two Semi-Circles Observed on the Complex Plane Plots on Porous Electrodes in the Presence of a Concentration Gradient. *J. Electroanal. Chem.* **2001**, 500 (1), 30–35.

30 Shin, H.-C.; Dong, J.; Liu, M. Nanoporous Structures Prepared by an Electrochemical Deposition Process. *Adv. Mater.* **2003**, 15 (19), 1610–1614.

31 Shin, H.-C.; Liu, M. Copper Foam Structures with Highly Porous Nanostructured Walls. *Chem. Mater.* **2004**, 16 (25), 5460–5464.

32 Shin, H.-C.; Liu, M. Three-Dimensional Porous Copper–Tin Alloy Electrodes for Rechargeable Lithium Batteries. *Adv. Funct. Mater.* **2005**, 15 (4), 582–586.

33 Cherevko, S.; Chung, C.-H. Impact of Key Deposition Parameters on the Morphology of Silver Foams Prepared by Dynamic Hydrogen Template Deposition. *Electrochim. Acta* **2010**, 55 (22), 6383–6390.

34 Li, Y.; Song, Y.-Y.; Yang, C.; Xia, X.-H. Hydrogen Bubble Dynamic Template Synthesis of Porous Gold for Nonenzymatic Electrochemical Detection of Glucose. *Electrochem. Commun.* **2007**, 9 (5), 981–988.

35 Cherevko, S.; Xing, X.; Chung, C.-H. Hydrogen Template Assisted Electrodeposition of Sub-Micrometer Wires Composing Honeycomb-like Porous Pb Films. *Appl. Surf. Sci.* **2011**, 257 (18), 8054–8061.

36 Yin, J.; Jia, J.; Zhu, L. Macroporous Pt Modified Glassy Carbon Electrode: Preparation and Electrocatalytic Activity for Methanol Oxidation. *Int. J. Hydrogen Energy* **2008**, 33 (24), 7444–7447.

37 Zhuo, K.; Jeong, M.-G.; Chung, C.-H. Highly Porous Dendritic Ni–Sn Anodes for Lithium-Ion Batteries. *J. Power Sources* **2013**, 244, 601–605.

38 Plowman, B. J.; Jones, L. A.; Bhargava, S. K. Building with Bubbles: The Formation of High Surface Area Honeycomb-like Films via Hydrogen Bubble Templated Electrodeposition. *Chem. Commun.* **2015**, 51 (21), 4331–4346.

39 Li, Y.; Jia, W.-Z.; Song, Y.-Y.; Xia, X.-H. Superhydrophobicity of 3D Porous Copper Films Prepared Using the Hydrogen Bubble Dynamic Template. *Chem. Mater.* **2007**, 19 (23), 5758–5764.

40 González-Buch, C.; Herraiz-Cardona, I.; Ortega, E.; García-Antón, J.; Pérez-Herranz, V. Study of the Catalytic Activity of 3D Macroporous Ni and NiMo Cathodes for Hydrogen Production by Alkaline Water Electrolysis. *J. Appl. Electrochem.* **2016**, 46 (7), 791–803.

41 Fan, M.; Garbarino, S.; Botton, G. A.; Tavares, A. C.; Guay, D. Selective Electroreduction of CO2 to Formate on 3D [100] Pb Dendrites with Nanometer-Sized Needle-like Tips. *J. Mater. Chem. A* **2017**, 5 (39), 20747–20756.

42 Ou, G.; Fan, P.; Zhang, H.; Huang, K.; Yang, C.; Yu, W.; Wei, H.; Zhong, M.; Wu, H.; Li, Y. Large-Scale Hierarchical Oxide Nanostructures for High-Performance Electrocatalytic Water Splitting. *Nano Energy* **2017**, 35, 207–214.

43 Hyun Ahn, S.; Choi, I.; Park, H.-Y.; Jun Hwang, S.; Jong Yoo, S.; Cho, E.; Kim, H.-J.; Henkensmeier, D.; Woo Nam, S.; Kim, S.-K.; Jang, J. H. Effect of Morphology of Electrodeposited Ni Catalysts on the Behavior of Bubbles Generated during the Oxygen

Evolution Reaction in Alkaline Water Electrolysis. *Chem. Commun.* **2013**, 49 (81), 9323–9325.

44 Hazlett, R. D. Fractal Applications: Wettability and Contact Angle. *J. Colloid Interface Sci.* **1990**, 137 (2), 527–533.

45 Shibuichi, S.; Onda, T.; Satoh, N.; Tsujii, K. Super Water-Repellent Surfaces Resulting from Fractal Structure. *J. Phys. Chem.* **1996**, 100 (50), 19512–19517.

46 Synytska, A.; Ionov, L.; Grundke, K.; Stamm, M. Wetting on Fractal Superhydrophobic Surfaces from "Core−Shell" Particles: A Comparison of Theory and Experiment. *Langmuir* **2009**, 25 (5), 3132–3136.

47 Doyle, R. L.; Godwin, I. J.; Brandon, M. P.; Lyons, M. E. G. Redox and Electrochemical Water Splitting Catalytic Properties of Hydrated Metal Oxide Modified Electrodes. *Phys. Chem. Chem. Phys.* **2013**, 15 (33), 13737–13783.

48 Zhang, C.; Qian, L.; Zhang, K.; Yuan, S.; Xiao, J.; Wang, S. Hierarchical Porous Ni/NiO Core–Shells with Superior Conductivity for Electrochemical Pseudo-Capacitors and Glucose Sensors. *J. Mater. Chem. A* **2015**, 3 (19), 10519–10525.

49 Trotochaud, L.; Young, S. L.; Ranney, J. K.; Boettcher, S. W. Nickel–Iron Oxyhydroxide Oxygen-Evolution Electrocatalysts: The Role of Intentional and Incidental Iron Incorporation. *J. Am. Chem. Soc.* **2014**, 136 (18), 6744–6753.

50 Bediako, D. K.; Lassalle-Kaiser, B.; Surendranath, Y.; Yano, J.; Yachandra, V. K.; Nocera, D. G. Structure–Activity Correlations in a Nickel–Borate Oxygen Evolution Catalyst. *J. Am. Chem. Soc.* **2012**, 134 (15), 6801–6809.

51 Corrigan, D. A. The Catalysis of the Oxygen Evolution Reaction by Iron Impurities in Thin Film Nickel Oxide Electrodes. *J. Electrochem. Soc.* **1987**, 134 (2), 377–384.

52 de Levie, R. In *AdVances in Electrochemistry and Electrochemical Engineering*; Delahay, P., Ed.; Interscience: New York, 1967; Vol. 6, p 329.

53 Mutha, H. K.; Lu, Y.; Stein, I. Y.; Cho, H. J.; Suss, M. E.; Laoui, T.; Thompson, C. V.; Wardle, B. L.; Wang, E. N. Porosimetry and Packing Morphology of Vertically Aligned Carbon Nanotube Arrays via Impedance Spectroscopy. *Nanotechnology* **2017**, 28 (5), 05LT01.

54 Hao, M.; Garbarino, S.; Prabhudev, S.; Borsboom-Hanson, T.; Botton, G. A.; Harrington, D. A.; Guay, D. Vertically Aligned Ni Nanowires as a Platform for Kinetically Limited Water-Splitting Electrocatalysis. *J. Phys. Chem. C* **2019**, 123 (2), 1082–1093.

55 Paasch, G.; Micka, K.; Gersdorf, P. Theory of the Electrochemical Impedance of Macrohomogeneous Porous Electrodes. *Electrochim. Acta* **1993**, 38 (18), 2653–2662.

56 Candy, J.-P.; Fouilloux, P.; Keddam, M.; Takenouti, H. The Characterization of Porous Electrodes by Impedance Measurements. *Electrochim. Acta* **1981**, 26 (8), 1029–1034.

57 Song, H.-K.; Jung, Y.-H.; Lee, K.-H.; Dao, L. H. Electrochemical Impedance Spectroscopy of Porous Electrodes: The Effect of Pore Size Distribution. *Electrochim. Acta* **1999**, 44 (20), 3513–3519.

58 Musiani, M.; Orazem, M.; Tribollet, B.; Vivier, V. Impedance of Blocking Electrodes Having Parallel Cylindrical Pores with Distributed Radii. *Electrochim. Acta* **2011**, 56 (23), 8014–8022.

59 Keiser, H.; Beccu, K. D.; Gutjahr, M. A. Abschätzung Der Porenstruktur Poröser Elektroden Aus Impedanzmessungen. *Electrochim. Acta* **1976**, 21 (8), 539–543.

60 Gourbeyre, Y.; Tribollet, B.; Dagbert, C.; Hyspecka, L. A Physical Model for Anticorrosion Behavior of Duplex Coatings. *J. Electrochem. Soc.* **2006**, 153 (5), B162–B168.

61 Itagaki, M.; Hatada, Y.; Shitanda, I.; Watanabe, K. Complex Impedance Spectra of Porous Electrode with Fractal Structure. *Electrochim. Acta* **2010**, 55 (21), 6255–6262.

62 Nguyen, P. H.; Paasch, G. Transfer Matrix Method for the Electrochemical Impedance of Inhomogeneous Porous Electrodes and Membranes. *J. Electroanal. Chem.* **1999**, 460 (1), 63–79.

63 McCrory, C. C. L.; Jung, S.; Peters, J. C.; Jaramillo, T. F. Benchmarking Heterogeneous Electrocatalysts for the Oxygen Evolution Reaction. *J. Am. Chem. Soc.* **2013**, 135 (45), 16977–16987.

64 Guo, C. X.; Li, C. M. Room Temperature-Formed Iron-Doped Nickel Hydroxide on Nickel Foam as a 3D Electrode for Low Polarized and High-Current-Density Oxygen Evolution. *Chem. Commun.* **2018**, 54 (26), 3262–3265.

65 Lu, X.; Zhao, C. Electrodeposition of Hierarchically Structured Three-Dimensional Nickel–Iron Electrodes for Efficient Oxygen Evolution at High Current Densities. *Nat. Commun.* **2015**, 6, 6616.

66 Dong, G.; Fang, M.; Zhang, J.; Wei, R.; Shu, L.; Liang, X.; Yip, S.; Wang, F.; Guan, L.; Zheng, Z.; Ho, J. C. In Situ Formation of Highly Active Ni–Fe Based Oxygen-Evolving Electrocatalysts via Simple Reactive Dip-Coating. *J. Mater. Chem. A* **2017**, 5 (22), 11009–11015.

67 Li, Y.; Yang, S.; Li, H.; Li, G.; Li, M.; Shen, L.; Yang, Z.; Zhou, A. Electrodeposited Ternary Iron-Cobalt-Nickel Catalyst on Nickel Foam for Efficient Water Electrolysis at High Current Density. *Colloids Surf., A* **2016**, 506, 694–702.

68 Fritz, W. Berechnung des maximalen volumens von dampfblasen. *Phys. Z.* **1935**, 36(11), 379-384.

SUPPLEMENTARY INFORMATION

Hydrogen Bubble Templating of Fractal Ni catalysts for Water Oxidation in Alkaline Media

M. Hao[1], V. Charbonneau[1], N. N. Fomena[1], J. Gaudet[1], D. R. Bruce[2], S. Garbarino[1], D. A. Harrington[3] and D. Guay[1]*

[1] Institut national de la recherche scientifique
Énergie, matériaux et télécommunications (INRS - EMT)
1650 Lionel Boulet Blvd.
Varennes, QC Canada J3X 1S2

[2] ZincNyx Energy Solutions Inc.
8765 Ash Street – Unit 1
Vancouver, BC Canada V6P 6T3

[3] Department of Chemistry,
University of Victoria, PO Box 1700,
Victoria, BC, Canada V8W 2Y2

* Corresponding author
Email: guay@emt.inrs.ca

Table of contents

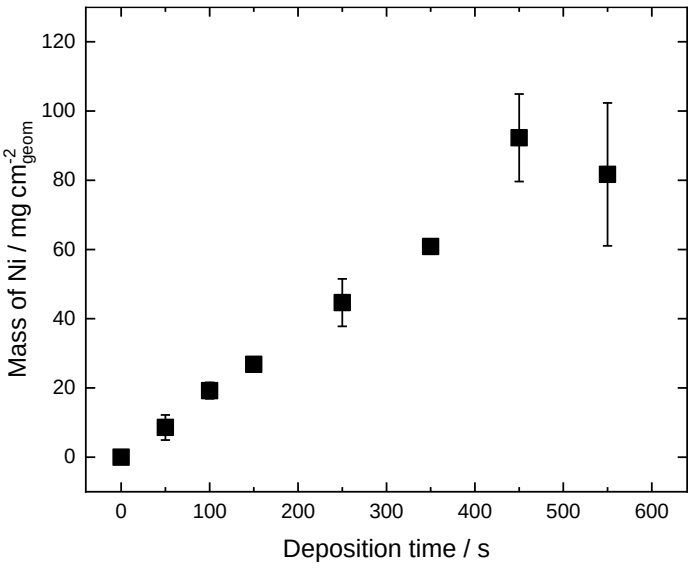

Figure S1 Effect of deposition times on the mass of Ni coatings. The substrate was a 1 cm^2 Ni plate in all cases.

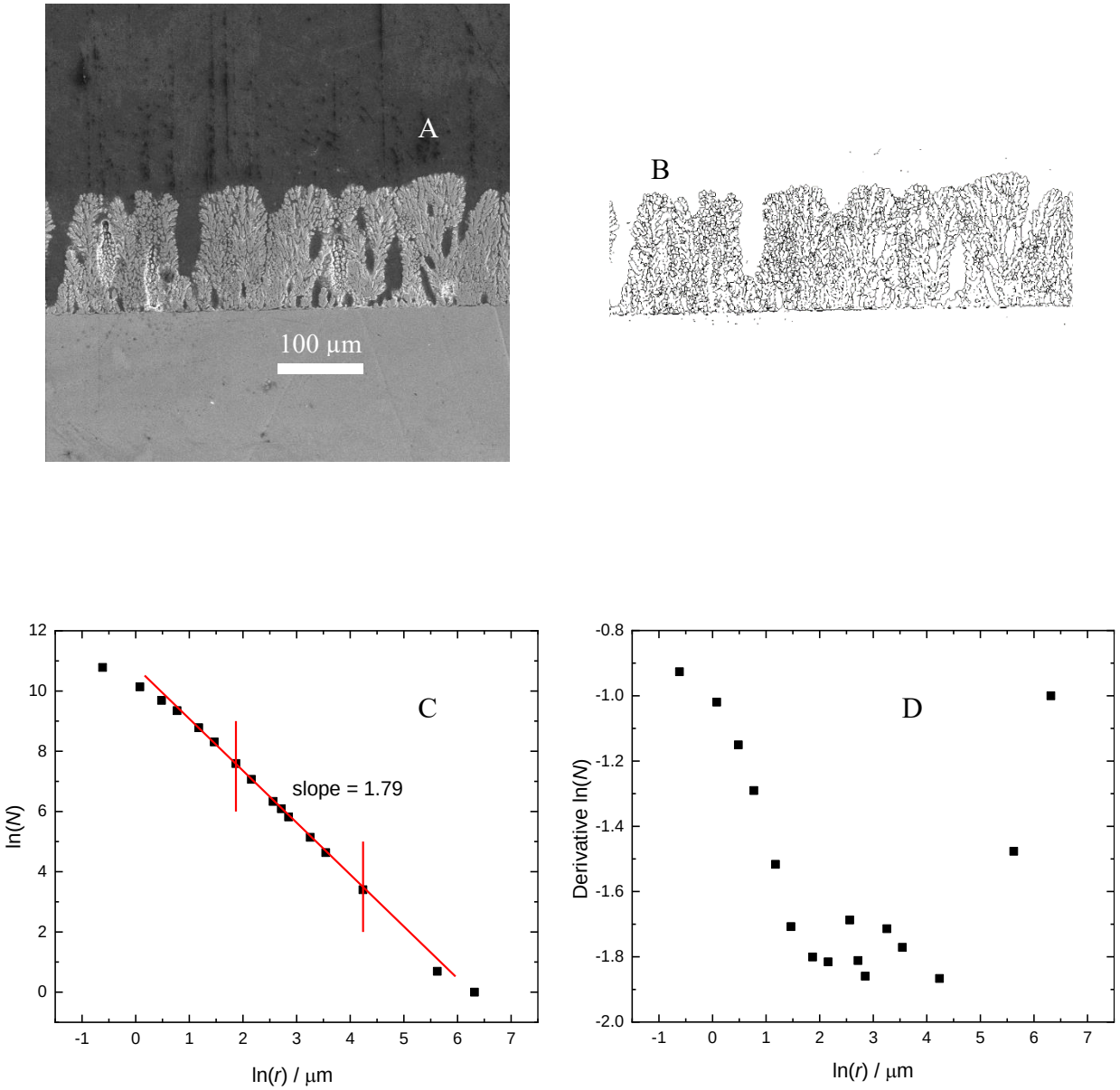

Figure S2 In (A), the original SEM cross-section image of a Ni_{DHBT} film (T_d = 450 s) at ×500 magnification. In (B), the contour image extracted from (A). In (C), ln – ln plot of box count N vs box size r. In (D), Derivative plot of ln(N) *vs* ln(r).

Fractal analysis

The SEM cross-section image of a Ni_{DHBT} sample (T_d = 450s) was taken at ×500 magnification as shown in Figure S2A. The original image was firstly converted to 8-bit grayscale

and then was segmented into features of interest and background by setting the threshold interval in-between 105 and 255. The structure's boundary was extracted by a Sobel edge detector in imagej software called ''find edge''. Then, the 2D contour image was skeletonized to one pixel wide. The final processed image is shown in Figure S2B.

The 2D contour fractal dimension was analyzed by the box counting tool in imagej. The box size was set between 1 to 1024 pixels which corresponds to a scale from 0.5 μm to 554 μm in the original image. The count of boxes containing pixels at different box sizes is presented in an ln-ln-plot (Figure S2C) of count N versus box size r. Over a certain local range of length scales the box count shows linear relationship with box size which means that porous metal materials appears to have obvious fractal characteristics. To determine the largest and the smallest size limits of the fractal behavior of the surface as well as the exact 2D fractal dimension, the derivatives of ln(N) in function of ln(r) were extracted from the ln-ln plot and is shown in Figure S2D. As a matter of fact, the derivative shows a plateau with a value of 1.79±0.05 in the interval of 6.49μm to 69.19 μm. Thus, the 2D fractal dimension D2 is estimated to be 1.79±0.05 and the upper and lower limit lengths of fractal behavior are 69.19 μm and 6.49 μm respectively. The fractal dimension D of the surface has been evaluated as $D = 2D + 1$=2.79. Then the value of $(L/l)^{D-2}$ mentioned in the main text is estimated to be 6.5.

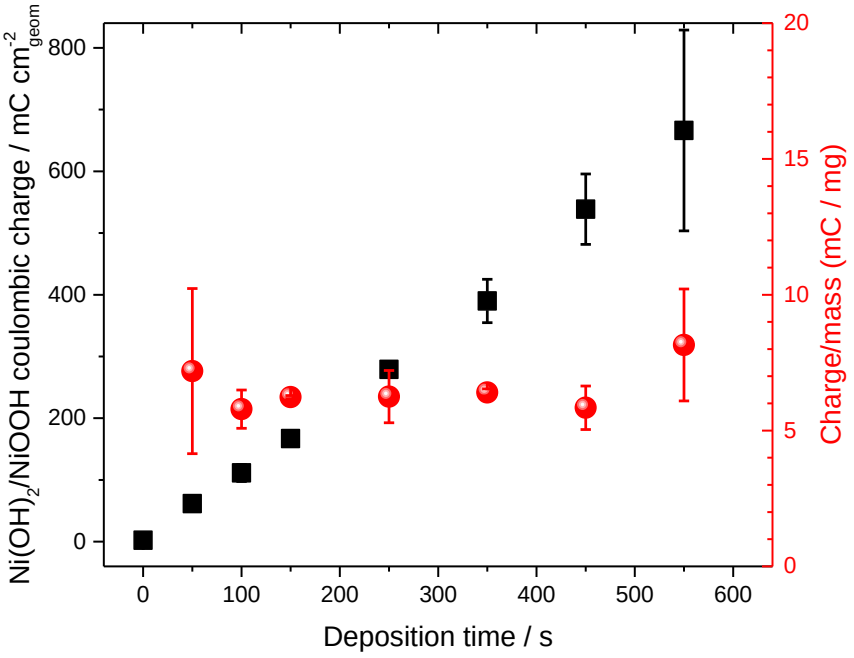

Figure S3 Effect of deposition times on the coulombic charge, Q_a, of the redox transition observed at *ca* 1.41 V, obtained from CV profiles recorded at 50 mV s^{-1} in 1 M KOH. The y-axis on the right-hand side displays the ratio between Q_a and the mass of the deposits. The fact that the Q_a / mass ratio doesn't vary with the deposition times indicates that the porous structure allows full access of the electrolyte to all the deposited material.

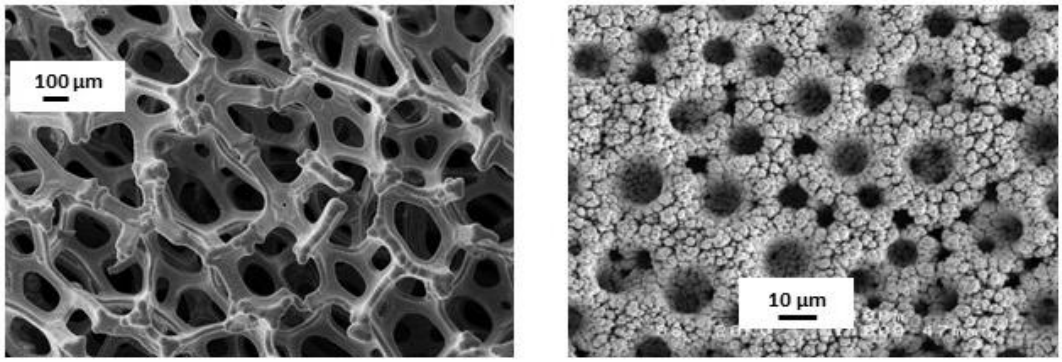

Figure S4 SEM micrographs of Ni foam (1mm thick) and NiDHBT film.

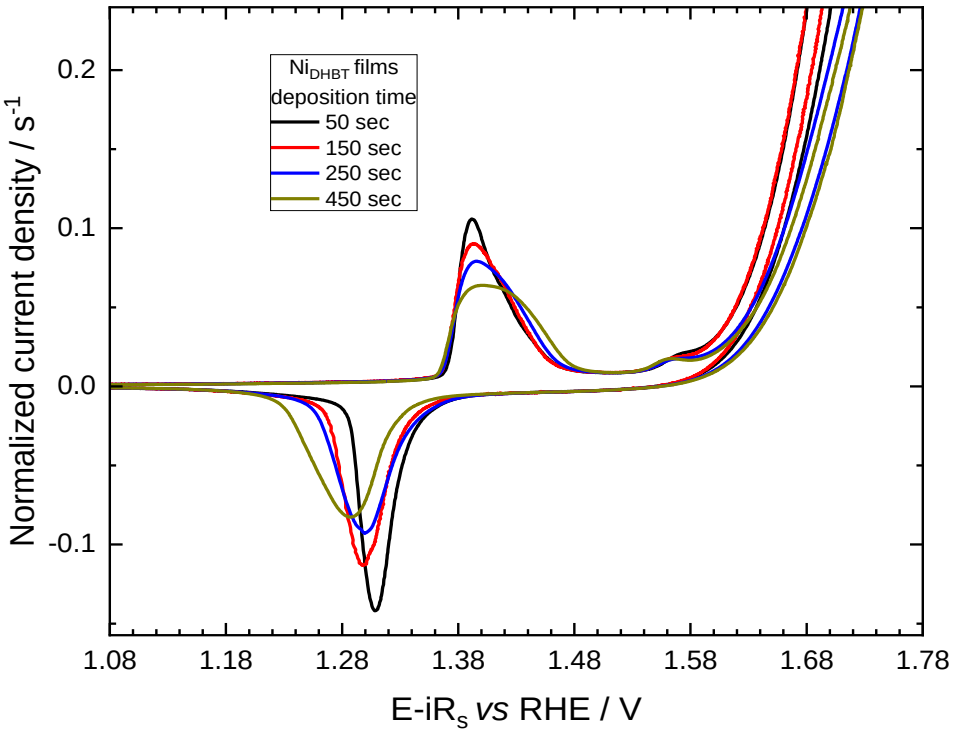

Figure S5 Normalized current density *vs* electrode potential curve. These curves were obtained following normalization of the CVs shown in Figure 2 by the corresponding Q_a values. The unit of the y-axis is thus s^{-1} and the area under the $Ni(OH)_2/Ni(OOH)$ redox transition has unit of V s^{-1}. Upon division by the scan rate (5 mV s^{-1}), the area under each $Ni(OH)_2/Ni(OOH)$ redox transition is dimensionless and has a value of 1.

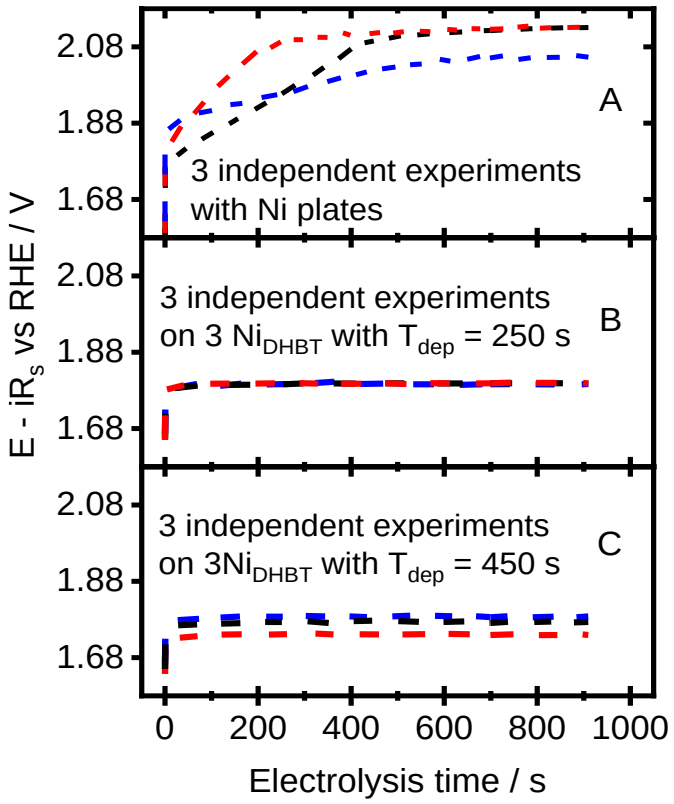

Figure S6 Chronopotentiometric curves at +250 mA cm^{-2} in 1 M KOH for different Ni plates and Ni$_{DHBT}$ electrodes; (A) Ni plates, (B) Ni$_{DHBT}$ with t_d = 250 s, and (C) Ni$_{DHBT}$ with T_d = 450 s. The error bars shown in Figure 3B were obtained from these measurements.

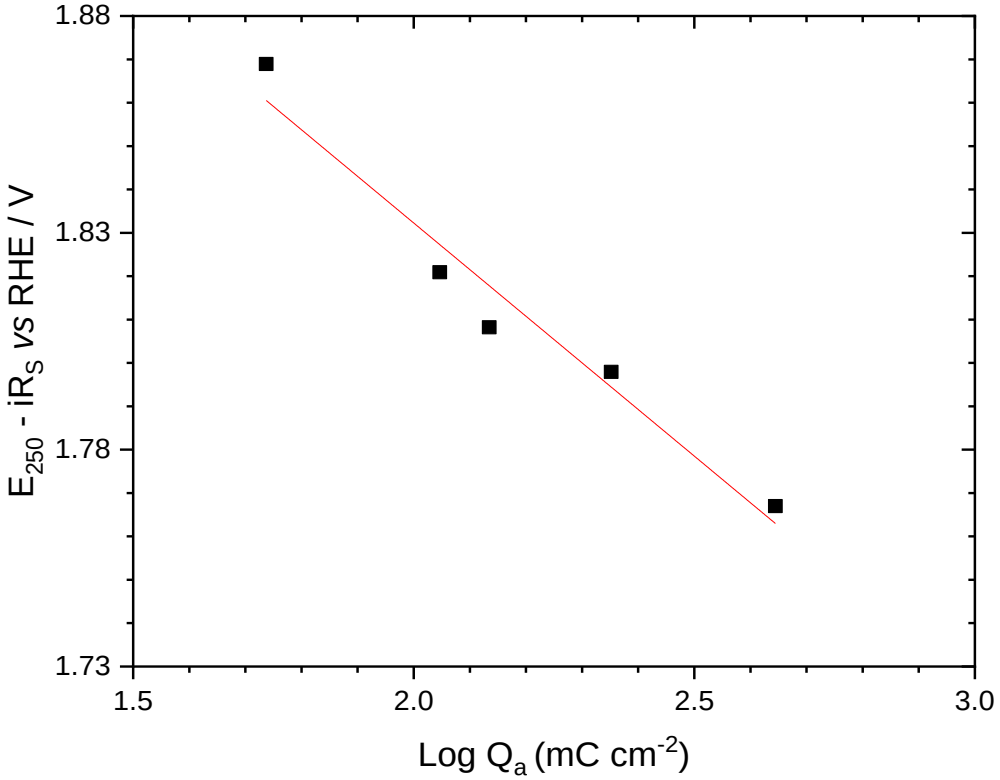

Figure S7 Variation of the *IR*$_s$-corrected electrode potential reached after 15 minutes of electrolysis at +250 mA cm^{-2} with respect to Q_a, the coulombic charge of the $Ni(OH)_2$/NiOOH transition.

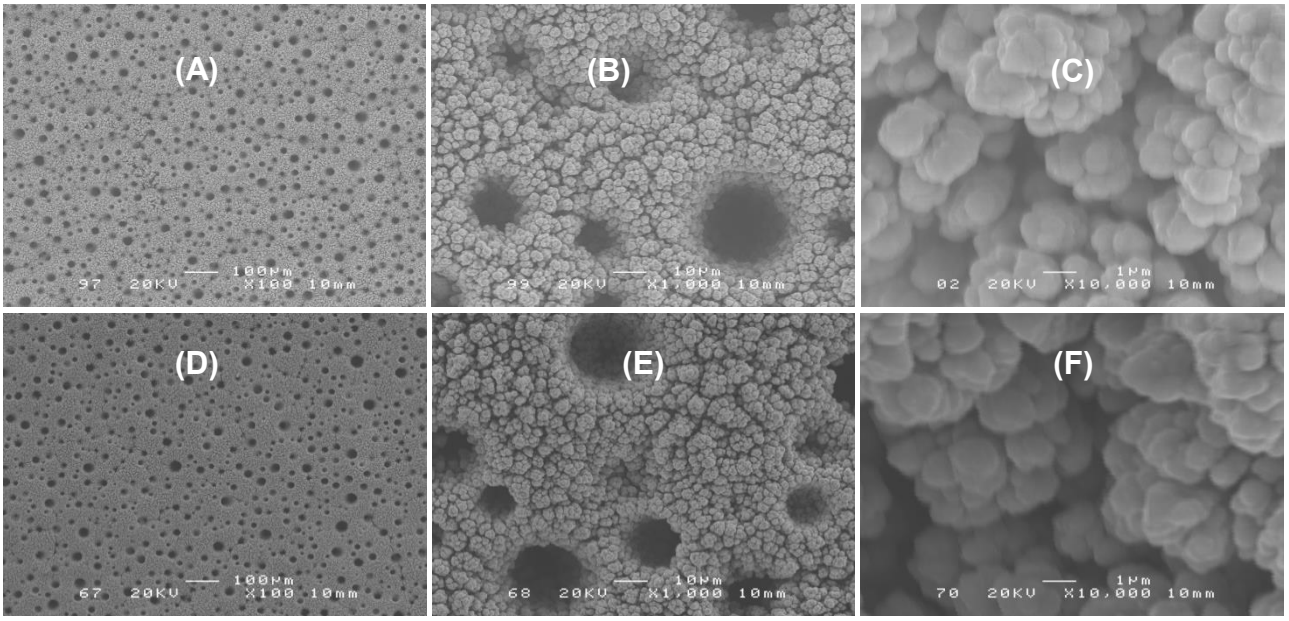

Figure S8 SEM images for Ni_{DHBT} films with T_{dep} = 450 s prior to (A, B and C) and after (D, E and F) polarization at 250 mA cm^{-2} for 15 min in 1M KOH. No morphological change due to strong O_2 gas evolution was observed.

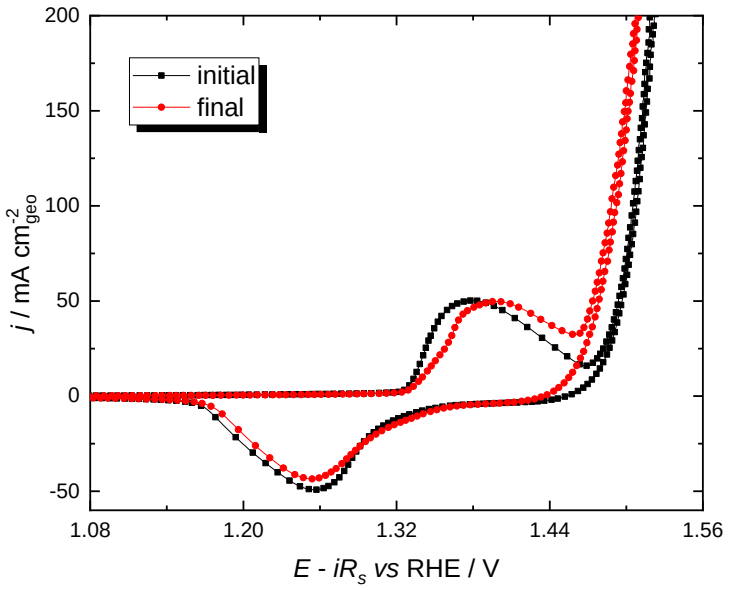

Figure S9 CVs of Ni_{DHBT} films with T_d = 450 s recorded before and after the data of Figure 5C were taken. The electrolyte was 1M KOH spiked with 10 ppm $FeCl_2$ and the CV profiles were recorded at 5 mV s^{-1}. The charge under the redox peaks centered at *ca* 1.39 V is hardly changed, although the shape of the oxidation and reduction peaks are slightly modified.